Check for updates

RESEARCH ARTICLE

NANO · MICRO small
www.small-journal.com

All-Metal Flexible Fiber by Continuously Assembling Nanowires for High Electrical Conductivity

Chengqiang Tang, Kailin Zhang, Sihui Yu, Hang Guan, Mingjie Cao, Kun Zhang, You Pan, Songlin Zhang, Xuemei Sun, and Huisheng Peng**

Fiber electronics booms as a new important field but is currently limited by the challenge of finding both highly flexible and conductive fiber electrodes. Here, all-metal fibers based on nanowires are discovered. Silver nanowires are continuously assembled into robust fibers by salt-induced aggregation and then firmly stabilized by plasmonic welding. The nanowire network structures provide them both high flexibility with moduli at the level of MPa and conductivities up to 10^6 S m^{-1}. They also show excellent electrochemical properties such as low impedance and high electrochemically active surface area. Their stable chronic single-neuron recording is further demonstrated with good biocompatibility in vivo. These new fiber materials may provide more opportunities for the future development of fiber electronics.

1. Introduction

Fiber electronics provide new opportunities for many important fields such as smart fabrics, health management, and biological monitoring.[1] Flexible fiber electrodes with high electrical conductivities are one of the foundations of its development. Among them, bulk metal wires are the most conductive,[2] but their intrinsic high moduli conflict with the need for flexibility in fiber electronics.

In order to realize the desired flexibility for fiber electrodes, the current strategy is to combine metal with non-conductive elastomers. For example, depositing metal films onto the surface of elastomeric fibers can obtain flexibility, but it requires multiple steps to obtain a conductive layer within a 360° range and faces problems of strain intolerance and shedding.[3] Wrapping metal wires on elastomer fibers can produce a more stable conductive layer, but it has inevitable gaps in the radial direction.[4] In addition, this strategy prevents the electrode from being thin enough, limiting many application scenarios such as our bodies. Blending metal fillers like nanowires and flakes with elastomers can easily make flexible fiber electrodes with controllable sizes.[5] However, the overall conductivity must be sacrificed because the non-conductive elastomer occupies a large volume to form a continuous phase to obtain the self-supporting fibers. Therefore, an ideal strategy is to design the metal itself into a self-supporting continuous phase for both high flexibility and conductivity.

Designing materials to mimic biological systems represents an attractive strategy.[6] As we know, fibers at the nanometer level such as collagen fibers form a continuous network in the extracellular matrix, endowing good mechanical properties.[7] Inspired by this, both highly flexible and conductive metal fiber may be realized entirely by assembling metal nanowires into a continuous network. Compared with bulk metal, electrical conductivity can be maintained as much as possible while flexibility can be improved significantly. However, it remains unavailable yet due to the weak interactions among adjacent metal nanowires during preparation, different from polymers and carbon-based nanowires.

Here, we present an all-metal fiber electrode (AFE) with both high flexibility and conductivity from silver nanowires (AgNWs) through an efficient wet spinning process lying in the saturated salt-induced aggregation and plasmonic welding (**Figure 1**a,b). With this strategy, we first solve the trade-off between stable dispersion and reliable continuous assembly of AgNWs, then introduce metallic bonds in situ for the strong interaction among the aggregated AgNWs by plasmonic welding, and finally achieve continuous fabrication of AFEs. Due to the formation of metallic bonds at the joints among AgNWs, the AFE is structurally stable and shows conductivity up to 6.2×10^6 S m^{-1}, much higher than the other flexible fiber electrodes. At the same time, the nanowire-based network structure gives AFE high flexibility with a low modulus of ≈200 MPa (three orders of magnitude lower than bulk structure). In addition, their electrochemical properties are far ahead of metal wire with bulk structure, having low impedance (≈1/20 of bulk structure at 1000 Hz), low cut-off frequency (two orders of magnitude lower than bulk structure), and high electrochemically active surface area (≈200 times of bulk structure). Finally, AFEs have been demonstrated as neural probes with good biocompatibility and stable chronic recording of single neurons. These results reveal the potential of AFEs as new flexible electrodes for fiber bioelectronics which can achieve long-term working in vivo with higher performances than bulk metals.

C. Tang, K. Zhang, S. Yu, H. Guan, M. Cao, K. Zhang, Y. Pan, S. Zhang, X. Sun, H. Peng
State Key Laboratory of Molecular Engineering of Polymers
Department of Macromolecular Science
Institute of Fiber Materials and Devices, and Laboratory of Advanced Materials
Fudan University
Shanghai 200438, China
E-mail: sunxm@fudan.edu.cn; penghs@fudan.edu.cn

The ORCID identification number(s) for the author(s) of this article can be found under https://doi.org/10.1002/smll.202405000

DOI: 10.1002/smll.202405000

 © 2024 Wiley-VCH GmbH

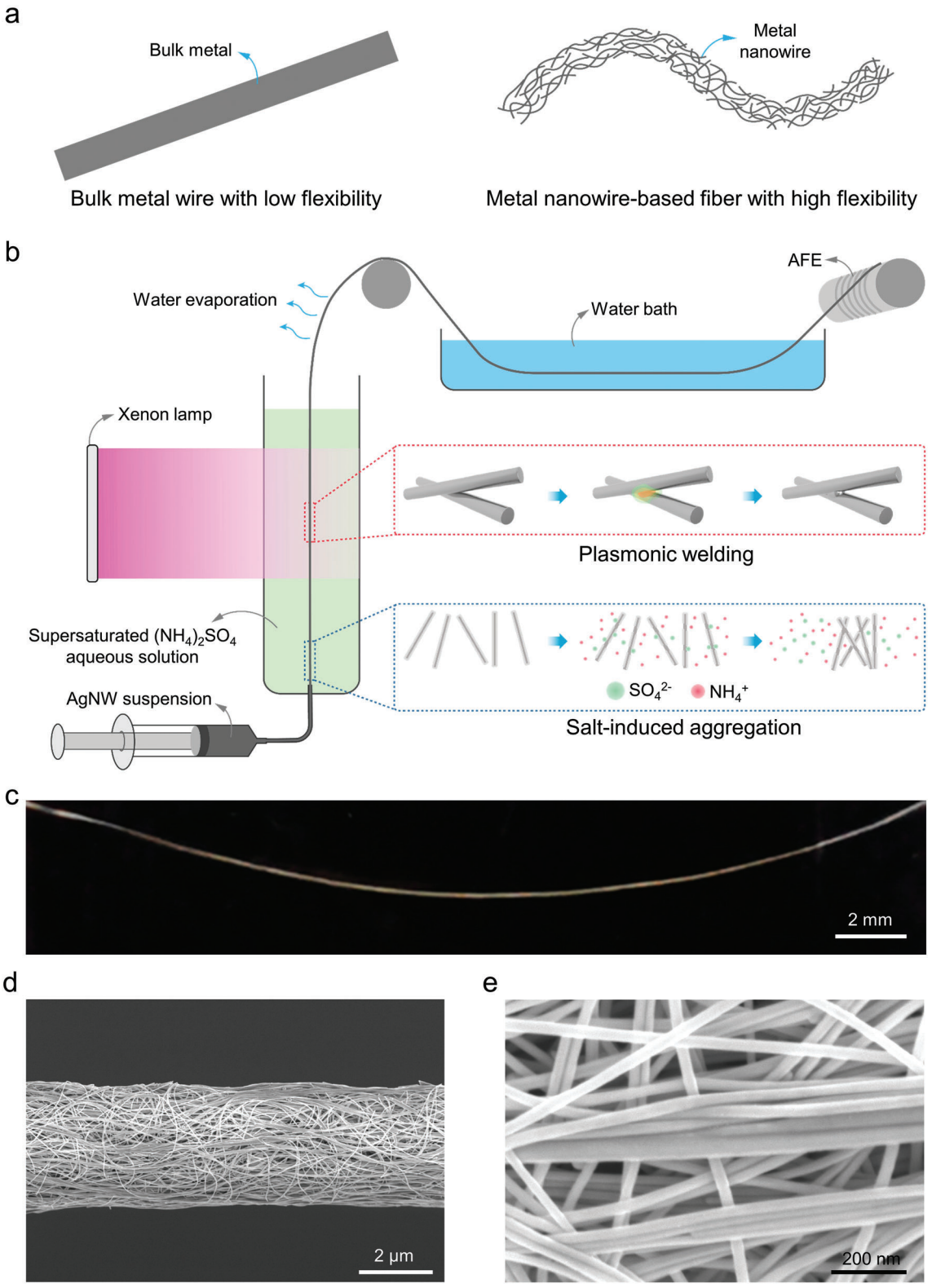

Figure 1. a) Schematic showing a general strategy for constructing conductive fibers based on metal nanowires rather than bulk metal to obtain high flexibility. b) Schematic diagram showing the continuous preparation of AFEs based on AgNWs through wet spinning, in which salt-induced aggregation and plasmonic welding of AgNWs are key chemical processes. c) Photograph of an AFE with high flexibility. d) FESEM image of a single AFE. e) A partially enlarged view of a single AFE showing the welded nanowire network.

© 2024 Wiley-VCH GmbH

16136829, 2024, 46, Downloaded from https://onlinelibrary.wiley.com/doi/10.1002/smll.202405000 by Fudan University, Wiley Online Library on [06/12/2024]. See the Terms and Conditions (https://onlinelibrary.wiley.com/terms-and-conditions) on Wiley Online Library for rules of use; OA articles are governed by the applicable Creative Commons License

Table 1. The impact of AgNW concentration on the spinning solution (C_{AgNW}), the salt concentration in the coagulation bath (C_{salt}), plasmonic welding, and extruding speed during preparation.

C_{AgNW} [mg mL^{-1}]	C_{salt} [mg mL^{-1}]	Plasmonic welding	Extruding speed [mm min^{-1}]	Result
5	500	Yes	20	No
5	Supersaturated	Yes	20	No
10	500	Yes	20	No
10	Supersaturated	Yes	20	No
20	500	Yes	20	No
20	Supersaturated	Yes	20	Yes
20	Supersaturated	No	20	No
20	Supersaturated	Yes	5	No
20	Supersaturated	Yes	100	No
40	Supersaturated	Yes	20	No

2. Results and Discussion

2.1. Continue Fabrication of AFEs

AgNW was selected as the building block for preparing the all-metal flexible fiber electrode as silver is the most conductive metal. Considering the efficiency, cost, and scalability, the wet spinning method was selected to make AFEs continuously. Polyvinylpyrrolidone (PVP)-cladded AgNWs were suspended in water to act as the spinning solution. Supersaturated ammonium sulfate [$(NH_4)_2SO_4$] aqueous solution was used as the coagulation bath, and the spinning solution was extruded into the coagulation bath from the bottom of the container. A xenon lamp with an emission spectrum ranging from 300 to 1100 nm was used for plasmonic welding. The welded fibers would reach the surface of the coagulation bath under the action of buoyancy, and AFEs were obtained after drying, washing, and second drying. The diameter of the single AFE was ≈3 µm, and AFEs with different diameters could be obtained by fusing multiple single AFEs in the water. When the two ends of the AFE were clamped with tweezers, it bent naturally and could also be easily wrapped around the glass capillary with a diameter of ≈500 µm (Figure 1c; Figure S1, Supporting Information). Furthermore, Field emission scanning electron microscopy (FESEM) images showed interconnected networks inside the AFE which ensured high flexibility (Figure 1d,e).

The key steps in preparing a structurally stable fiber lie in the continuous aggregation of AgNWs and the formation of strong interaction among them. Corresponding to the specific process, it relied on the cooperation among AgNW concentration in spinning solution, ion concentration in coagulation bath, plasmonic welding, and extruding speed (**Table 1**). On the one hand, the low concentration of AgNW in the spinning solution made the system more stable and could be easily extruded out of the needle without clogging. On the other hand, a high concentration was necessary for forming enough overlap joints when AgNWs in the spinning solution were aggregated in the coagulation bath. After optimization, the concentration of AgNWs was 20 mg mL^{-1}. Before the spinning solution entered the coagulation bath, the AgNW was cladded by a PVP layer with low surface energy and negative potential of ≈28 mV (Figure S2, Supporting Information), which inhibited the aggregation of the AgNWs and ensured the stable dispersion before wet spinning (Figures S3 and S4, Supporting Information).[8] After entering the coagulation bath, $(NH_4)_2SO_4$ interacted with PVP, detaching it from the AgNW surface. Subsequently, the high surface energy and small negative potential (≈2.6 mV) induced the AgNWs to aggregate along with the addition of $(NH_4)_2SO_4$ (Figure S5, Supporting Information).[9] Thus, the initial fiber with overlapping joints inside was obtained.[10] A high salt concentration in a coagulation bath could prevent excessive AgNWs from detaching from the initial fiber. UV–vis spectroscopy showed that when the salt concentration in the coagulation bath increased from 5 to 20 mg mL^{-1}, fewer AgNWs were dispersed (**Figure 2**a).

Since solvent exchange took longer than the aggregation, the newly formed initial fibers would float up, induced by buoyancy, and were subjected to the surrounding water pressure to ensure the overlapping structure did not fall apart. During this process, light with wavelengths ranging from 300 to 1100 nm was illuminated on the initial fiber. Plasmon of the AgNWs was excited by the light and a giant local field (E) around them was generated (Figure 2b) to induce local heating which is proportional to the square of the local field.[11] Finally, reliable plasmonic welding at the overlap joints among AgNWs was achieved in situ based on the above heating.

To verify the reliability of plasmonic welding, we placed the initial fiber and the welded fiber into deionized water and shook the container. The result showed that the latter remained stable while the former underwent structural collapse. FESEM results showed that welding joints contributed to the above stability (Figure 2c). Furthermore, the initial fibers could no longer leave the deionized water to form self-standing fibers even without shaking because the physical contact joints could not overcome the surface tension of water. At the same time, we took some residue solutions from the container to obtain UV–vis spectra and no characteristic peaks of AgNWs were observed for the welded fiber group, indicating welded joints were reliable and AgNWs were stably maintained in overall fibers (Figure 2d). Therefore, the welded fiber has sufficient mechanical strength to ensure that it can overcome the surface tension of the liquid and smoothly cross the liquid–gas interface for continuous spinning.

Furthermore, we have characterized the joints for initial and welded fibers through cryogenic transmission electron microscopy (cryo-TEM). We observed the microstructure of the initial fiber overlap joints. The result showed that adjacent contacting AgNWs in initial fibers had gaps between them, and obvious discontinuous lattice stripes were observed, indicating that they remain independent. While there were continuous lattice stripes on the joints of AgNWs in the welded fiber, with a stripe spacing of 2.36 Å matching the crystal plane of silver (1 1 1). Therefore, light field-induced plasmonic welding generated continuous metal bonds in the welding joints (Figure 2e) to ensure the stable structure of AFE.

2.2. Mechanical and Electrical Performances of AFEs

The mechanical properties of AFE could then be adjusted by changing the extruding speed. The greater the extruding speed,

 © 2024 Wiley-VCH GmbH

16136829, 2024, 46, Downloaded from https://onlinelibrary.wiley.com/doi/10.1002/smll.202405000 by Fudan University, Wiley Online Library on [06/12/2024]. See the Terms and Conditions (https://onlinelibrary.wiley.com/terms-and-conditions) on Wiley Online Library for rules of use; OA articles are governed by the applicable Creative Commons License

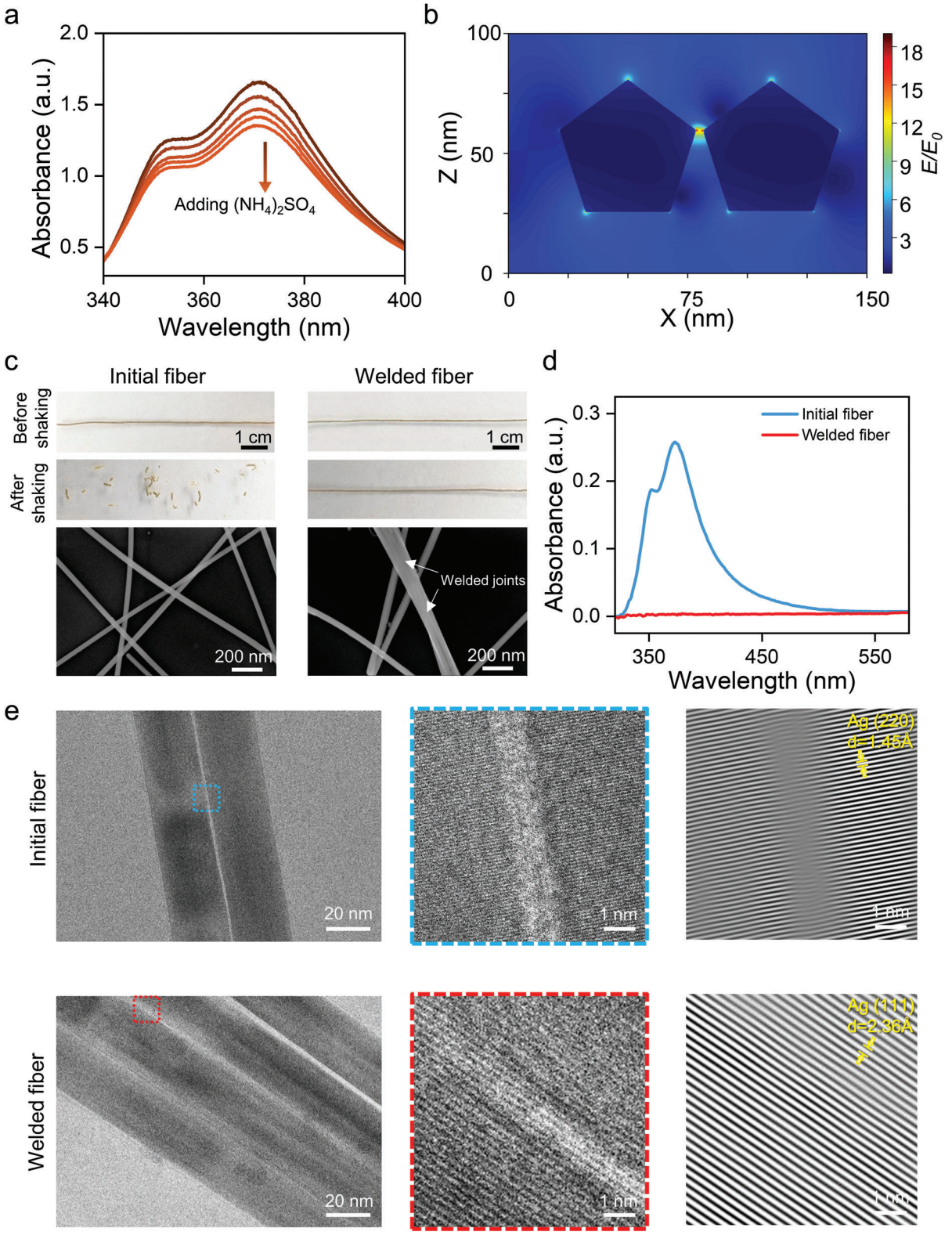

Figure 2. a) UV–vis absorption spectra of the AgNW suspension after adding different amounts of ammonium sulfate. b) Finite difference time domain simulations of the electric field distribution around AgNWs under 570 nm incident light. c) Structural stability of initial fibers and welded fibers in water. The structure of the welded fiber was stable in water, and an FESEM image was obtained after mechanical destruction. d) UV–vis absorption spectra of water after initial fiber and welded fiber soaked and shaken. e) Cryo-TEM images of AgNWs in the initial and welded fibers. From left to right: two parallel AgNWs in contact with each other, a partially enlarged view of contact position, lattice fringe morphology obtained by Fourier transform.

© 2024 Wiley-VCH GmbH

16136829, 2024, 46, Downloaded from https://onlinelibrary.wiley.com/doi/10.1002/smll.202405000 by Fudan University, Wiley Online Library on [06/12/2024]. See the Terms and Conditions (https://onlinelibrary.wiley.com/terms-and-conditions) on Wiley Online Library for rules of use; OA articles are governed by the applicable Creative Commons License

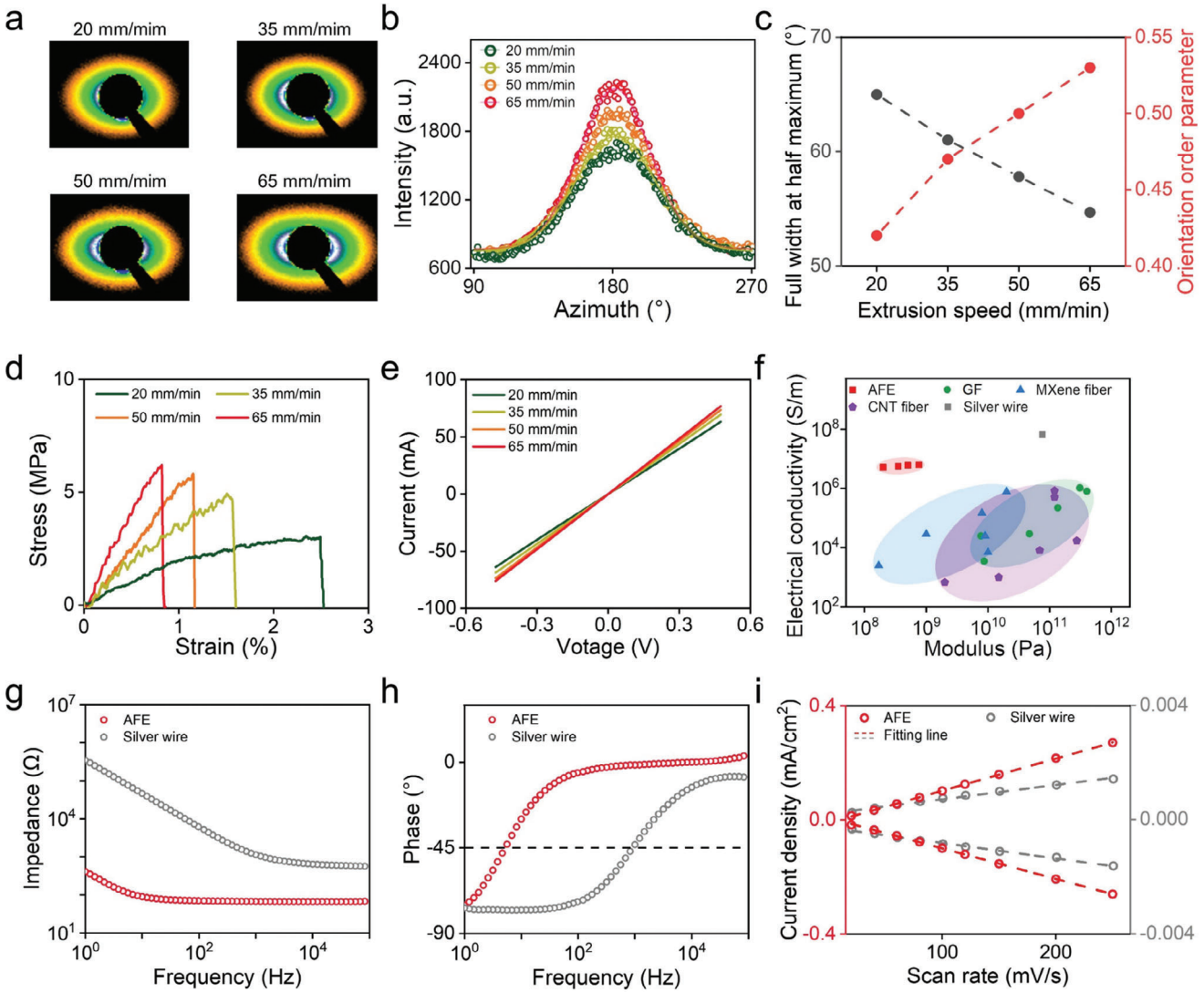

Figure 3. a) 2D SAXS patterns of AFEs prepared with different extruding speeds. b) Fitting curves of scattering intensity as a function of azimuth angle obtained by integrating the patterns. c) The full width at half maximum of the fitting curves in Figure (b) and the orientation coefficient calculated based on the fitting curves. d) Typical stress-strain curves of AFEs. (e) Typical *I*–*V* curves of AFEs. f) Ashby-style plot comparing electrical conductivity (5.2–6.2 × 10^6 S m^{-1}) and moduli (201–762 MPa) of AFE with other general fiber electrodes. g) The impedances of AFE and metal wire at different frequencies. h) Phase plots of AFE and metal wire. The intersection between the phase plot and the grey dashed line corresponds to the cut-off frequency. i) The double layer charging currents at different scan rates of the AFE and metal wire.

the greater the shear force experienced by the AgNWs in the spinning solution, and the easier the AgNWs were to orient in AFE to show high strength. On the one hand, the extruding speed could not be too slow because the spinning solution would solidify before it left the needle. On the other hand, the extruding speed could not be too fast because the solidification speed would not keep up with the extruding speed to obtain the self-supporting initial fiber. Thus, we selected four extruding speeds of 20, 35, 50, and 65 mm min^{-1}. And the Reynolds number was less than 1, indicating high laminar flow, which guarantees stable extruding (Figure S6; Movie S1, Supporting Information). The small angle X-ray scattering (SAXS) results showed that the orientation order parameter of AFEs increased from 0.42 to 0.53 when the extruding speed increased from 20 to 65 mm min^{-1} (**Figure 3**a–c; Figure S7, Supporting Information). The resulting AFEs were subjected to the tensile test, and the results showed that as the degree of orientation increased, the elongation at breaking decreased from 2.5% to 0.8%, but the modulus increased from 201 to 762 MPa (Figure 3d). We further took AFEs with the lowest modulus as examples and tested the bending force, bending stress, and bending stiffness, which were much lower than those of bulk metal wire, showing better flexibility of AFEs (Figures S8 and S9, Supporting Information).

Although the mechanical properties have been changed through extruding speeds, the electrical conductivity was maintained. The lowest and highest conductivity values for the above orientation degrees were 5.2 × 10^6 and 6.2 × 10^6 S m^{-1}, respectively (Figure 3e). This allowed us to make AFEs with different

© 2024 Wiley-VCH GmbH

16136829, 2024, 46, Downloaded from https://onlinelibrary.wiley.com/doi/10.1002/smll.202405000 by Fudan University, Wiley Online Library on [06/12/2024]. See the Terms and Conditions (https://onlinelibrary.wiley.com/terms-and-conditions) on Wiley Online Library for rules of use; OA articles are governed by the applicable Creative Commons License

moduli to match more application scenarios without sacrificing electrical conductivity. And AFEs could also maintain stable conductivity when they were bending with different angles up to 150° (Figure S10, Supporting Information). To sum up, the AFE we prepared had a modulus three orders of magnitude lower while its conductivity was just one order of magnitude lower than that of bulk silver wire. Furthermore, AFE still exhibited obvious advantages in both modulus and conductivity compared with other typical flexible conductive fibers based on nanomaterial assembly strategies, e.g., graphene fiber (GF), MXene fiber, and carbon nanotube (CNT) fiber (Figure 3f).[12] And the tensile strengths of AFEs were at the MPa level, which was lower than that of the above comparison samples (Figure S11, Supporting Information).

Compared with bulk metal wires, the nanowire network structure in the AFE brought a larger specific surface area (>10 $m^2\ g^{-1}$). It had pores of different sizes at the nanoscale, among which the ones of ≈50 nm accounted for the largest proportion (Figure S12, Supporting Information). As a result, the AFE exhibited lower impedance than bulk metal wires. For example, values of them were ≈67 Ω and ≈1142 Ω at 1000 Hz (Figure 3g). At the same time, the phase plot showed that the AFE had a lower frequency (≈5 Hz) at –45° than the bulk metal wire (≈900 Hz), which meant it had a lower cutoff frequency (Figure 3h). These made AFEs suitable for high-fidelity detection and transmission of electrical signals in vivo of various frequencies such as neural signals.[13] Furthermore, cyclic voltammetry results at different scan rates showed that the AFE had an electrochemically active surface area as ≈314 for 1 mm^2 geometric area, which was ≈200 times higher than that of bulk metal wires (Figure 3i; Figure S13, Supporting Information), allowing AFEs to be applied in more scenarios such as flexible electrochemical sensors.

2.3. Biocompatibility and Electrophysiology Application of AFEs

Using electrodes to record neural signals in the brain is a basic method for studying the brain, and high electrical conductivity is necessary for neural electrodes to capture high-speed (>1000 Hz) single-unit spikes.[14] As a demonstration, we implanted the side-insulated AFE into the brains of mice as neural electrodes. Note that a layer of gold was deposited on the outside of the AgNWs in the AFE to protect the silver from corrosion when it was used in vivo. Compared with high-modulus bulk metal wire, AFE could achieve stable recording of chronic neural signals (**Figure 4a**). Immunological results showed that AFE activated fewer glial cells and damaged fewer neurons than bulk metal wire (Figure 4b).

Furthermore, we implanted the AFE-based neural electrode into the olfactory bulb of mice and evaluated its ability to track and record single neuron signals for the long term (Figure 4c). During the first week, AFE recorded two single-neuron signals. By the second week, as the surrounding nerve tissue recovered, another single-unit spike was recorded. The three single-unit spikes remained stable as the implantation time increased (Figure 4d). Interspike interval (ISI) distributions and principal component analysis (PCA) also demonstrated the stability of the records (Figure 4e). Finally, we demonstrated the potential of AFE for brain function studies during chronic recording. The activity of the olfactory bulb is closely related to the perception of odor in animals. Isoamyl acetate was used as odor stimulation for the anesthetized mouse. Single-unit spikes with high firing rates were observed when the isoamyl acetate was added into the airway. The firing rate of recorded spikes was approximately reduced by half when the isoflurane concentration increased from 0.5% to 1.0%. Moreover, it was less than one-fifth of the initial state when the isoflurane concentration increased to 2.0%, i.e., high-concentration isoflurane inhibited the odor stimulation (Figure 4g).

3. Conclusion

In conclusion, we obtained all-metal flexible conductive fibers by continuously assembling AgNWs combined with salt-induced aggregation and plasmonic welding during wet spinning. The resulting fibers inherited the high conductivity of metals to the greatest extent, while their modulus was reduced to the MPa level for high flexibility. Additionally, they exhibited electrochemical properties that were much higher than those of bulk metal wires. We have further verified the fibers' biocompatibility and ability to record stably single neuron signals over a long period in mouse brains. These fibers will act as reliable flexible substrates to develop fiber electronics with higher performances.

4. Experimental Section

Preparation of AFEs: The AgNW suspension was purchased from Zhejiang Xinglong New Material Technology Co., Ltd. with a concentration of 10 mg mL^{-1}. The spinning solution with a concentration lower than 10 mg mL^{-1} was obtained by diluting it with deionized water. The spinning solution with a concentration higher than 10 mg mL^{-1} was obtained by removing the supernatant after centrifugation. 100 g of ammonium sulfate (Sinopharm Chemical Reagent Co., Ltd.) was added to 100 mL of deionized water and stirred thoroughly to obtain a saturated ammonium sulfate solution as a coagulation bath. The prepared spinning solution was inhaled into a 1 mL syringe, then it was put into the syringe pump. The silicone tube was used to connect the syringe and the 30 G needle which was inserted into the bottom of the coagulation bath. A xenon lamp (SM-7052, Zhejiang Shishi Lighting Co., Ltd.) was used to illuminate the area above the needle. The single AFE was obtained after the winding device pulled the fiber through a sequence of drying, washing, and drying processes. The extruding speed actively matched the winding speed. AFEs with different diameters can be obtained by fusing multiple single AFEs through water.

A chemical gold plating strategy was used to modify the AFE surface with nano-gold layers to prevent the leakage of silver ions.[15] First, the gold seed solution was prepared: 1.4 mL tetrachloroauric acid trihydrate (Aladdin Biochemical Technology Co., Ltd.) aqueous solution (0.25 M), 8.4 mL sodium hydroxide aqueous solution (0.2 M) and 105 mL sodium sulfite (Sinopharm Chemical Reagent Co., Ltd.) aqueous solution (0.01 M) were mixed and left at room temperature for 12 h. Then the growth solution was prepared: 14 mL sodium hydroxide (Sinopharm Chemical Reagent Co., Ltd.) aqueous solution (0.5 M), 14 mL L-ascorbic acid (Aladdin Biochemical Technology Co., Ltd.) aqueous solution (0.5 M), 3.5 mL sodium sulfite (Sinopharm Chemical Reagent Co., Ltd.) aqueous solution (0.1 M) and 320 mL deionized water were mixed and left at room temperature for 2 h.

AFEs were suspended and fixed on the glass scaffold, and there was no contact between adjacent fibers. The scaffold was then slowly immersed into the growth solution, and then the gold seed solution was poured into the growth solution along the beaker wall. The whole process lasted for 1 h, the mixed solution remained transparent or light orange, and the AFE surface gradually changed from gray to orange. After the above process

© 2024 Wiley-VCH GmbH

16136829, 2024, 46, Downloaded from https://onlinelibrary.wiley.com/doi/10.1002/smll.202405000 by Fudan University, Wiley Online Library on [06/12/2024]. See the Terms and Conditions (https://onlinelibrary.wiley.com/terms-and-conditions) on Wiley Online Library for rules of use; OA articles are governed by the applicable Creative Commons License

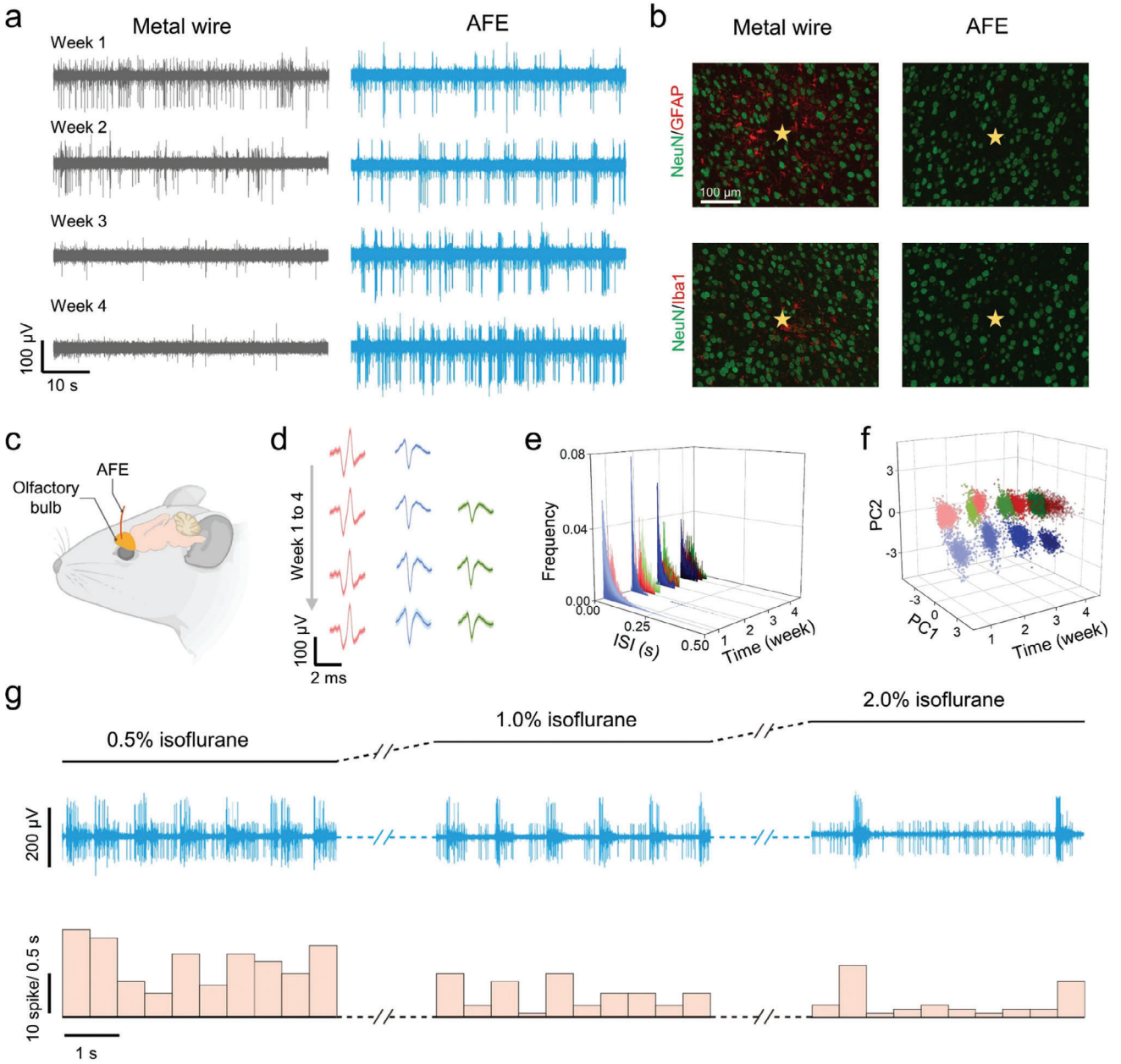

Figure 4. a) Chronic neural recording performed by the metal wire and AFE. Bandpass-filtered signals were shown here. b) Immunohistochemical images stained with neuron (NeuN, green), astrocyte (GFAP, red), and microglial (Iba1, red) markers of brain slices implanted with metal wires and AFEs for 4 weeks. The yellow star indicates the position of the implants. c) Schematic showing the AFE was implanted into the olfactory bulb for chronic neural recording. d) Single-unit spike tracking by the AFE from week 1 to 4 post-implantation. e) ISI distributions of the recorded spikes. f) PCAs of the recorded spikes. g) Single-unit recording of olfactory bulb neurons in the anesthetized mice during odor stimulation (isoamyl acetate). The neuron's firing rate can be altered by changing the concentration of isoflurane.

was completed, the glass scaffold was taken out and repeatedly soaked in deionized water three times to clean the surface of AFEs.

Structural Characterization: Field emission scanning electron microscopy (FESEM, Ultra 55, Zeiss) was used to observe the microstructure with a voltage of 3 kV. Cryogenic transmission electron microscopy (cryo-TEM, Cryo ARM 300, JEOL) was used to observe the welding structure of AgNWs at a voltage of 100 kV. Software DigitalMicrograph was used to perform Fourier transformation on the lattice fringe images. The macroscopic morphology of the sample was photographed with a digital camera. The small angle X-ray scattering (SAXS, Xeuss 2.0, Xenocse) was used to characterize the orientation degree of AFEs. The spot size was 1 mm. Multiple fibers were stacked in parallel on the polyimide tape for testing. The scattering intensity of the obtained 2D scattered pattern in the circumferential direction was integrated to obtain the change of intensity with azimuth angle. The full width at half maximum was obtained after Gaussian fitting. Maier–Saupe distribution function fitting was performed on the obtained scattering intensity versus azimuth angle distribution curve to calculate the orientation coefficient f to quantify the micromorphology of the

© 2024 Wiley-VCH GmbH

16136829, 2024, 46, Downloaded from https://onlinelibrary.wiley.com/doi/10.1002/smll.202405000 by Fudan University, Wiley Online Library on [06/12/2024]. See the Terms and Conditions (https://onlinelibrary.wiley.com/terms-and-conditions) on Wiley Online Library for rules of use; OA articles are governed by the applicable Creative Commons License

AFEs.[16] The value range of f was 0–1, where 0 represented an isotropic structure, and 1 represented a perfectly arranged structure along the orientation direction. The calculation process was as follows:

$$I = I_0 + A\exp\left[\omega\cos^2(\varphi - \varphi_0)\right] \quad (1)$$

I_0 was the free baseline intensity, φ_0 was the azimuth angle where the maximum scattering intensity was located, φ represented the azimuth angle, and ω was the distribution width parameter. The parameters I_0, A, and ω could be determined by fitting the intensity azimuth angle curve with this function. Then the orientation coefficient f was calculated by the following formula:

$$f = \frac{\int_{-1}^{1} P_2(\cos\varphi)\exp\left(\omega\cos^2\varphi\right) d(\cos\varphi)}{\int_{-1}^{1}\exp\left(\omega\cos^2\varphi\right) d(\cos\varphi)} \quad (2)$$

$$P_2(\cos\varphi) = \frac{1}{2}\left(3\cos^2\varphi - 1\right) \quad (3)$$

A specific surface area and porosity analyzer (ASAP2460, Micromeritics) were used to characterize the specific surface area and pore size distribution of the AFE sample through nitrogen adsorption–desorption isotherms.

Dispersion Test of AgNWs: UV–vis spectroscopy (Lambda750, Perkin–Elmer) was used to characterize the concentration of AgNWs in the solution. The sample to be tested was diluted to a translucent state and then placed into a quartz cuvette for testing, with a spectral range of 300–600 nm. During the test, a certain amount of salt was added to the cuvette several times. After waiting for the salt to completely dissolve each time, let it sit for 1 min before testing. A zeta potential analyzer (ZS90, Malvern Instruments) was used to characterize the zeta potential of the samples. Rheological properties were characterized by a rotational rheometer (MCR 302, Anton Paar) with shear rates ranging from 0.01 to 100 s^{-1}.

Finite Difference Time Domain Simulations: The finite difference time domain simulation was performed by a commercial software, Lumerical Solutions (Canada) to predict the electric field distribution around AgNWs under incident light. A geometric model of AgNWs (pentagonal prism with an inscribed circle diameter of 30 nm and a length of 6 µm) was constructed in a vacuum medium through which a plane wave from 300 to 600 nm was transmitted. The refractive indices of materials were taken from the literature.[10] The perfectly matched layer condition was assumed in the propagation direction (z) and periodic boundary conditions were chosen in the two transversal directions (x and y). The space was discretized with a resolution of 0.1 nm. The simulated field can be expressed by the following formula:

$$E = \frac{E_0(\varepsilon_1 - \varepsilon_0) D^2}{4(\varepsilon_1 + \varepsilon_0) d^2} \quad (4)$$

where, E, E_0, ϵ_0, and ϵ_1 are the field of the scattered light, the field of the incident light, permittivity of the air, and the permittivity of the AgNW, respectively. D is the diameter of the AgNW, and d is the distance from the AgNW center. The heat converted from the light adsorbed can be calculated in terms of the following formula:

$$q = 0.5n^2\omega Im(\varepsilon_1)|E|^2 \quad (5)$$

where q is the volumetric heat source density inside the AgNWs, n is the refractive index of the surroundings, and ω is the angular frequency of the external field.[10]

Mechanical Performance Tests: A universal mechanical testing machine (Instron 3365, Instron) was used to test the stress–strain curve of the AFE with a tensile speed of 2 mm min^{-1}. The bending stress of the AFE was measured by fixing one end of the fiber to the upper clamp and moving it vertically toward a fixed disk below at a speed of 2 mm min^{-1}.

Electrical Performance Tests: A digital source meter (2400, Keithleye) was used to test the *I–V* curve and conductivity of the sample. Both ends of the fiber sample were connected to conductive copper tape by conductive silver paste. An electrochemical workstation was used to test the electrochemical properties of the samples, using three electrodes system. The sample was used as the working electrode, the silver/silver chloride electrode was used as the reference electrode, and the platinum wire electrode was used as the counter electrode. The electrolyte was 1 × PBS solution (Servicebio). The impedance scanning range was 1–100 000 Hz. For the electrochemical active surface area test (ECSA), 0.1 M KF (Aladdin Biochemical Technology Co., Ltd.) aqueous solution purified by nitrogen was used as the electrolyte, the mercury oxide electrode was used as the reference electrode, the scanning range was 0.15–0.25 V, and the scanning speed was gradually increased from 20 to 250 mV s^{-1}. The maximum double-layer charging current at different scan rates was plotted, and a linear regression analysis was performed to determine the slope of the fitted line. This slope represents the double-layer capacitance of each sample. Since the double-layer capacitance is directly proportional to the roughness of the electrode within a potential range where no faradaic reactions occur, it can be used as an estimation for ECSA. By dividing the obtained double-layer capacitance by a value of 0.25 F m^{-2} which is typical for Ag with a planar surface, the ECSA could be obtained for each sample.[17]

Assembly of AFE-Based Neural Electrodes: First, a polydimethylsiloxane (PDMS) precursor (SYLGARD184, Dow Corning) mixture (A:B 1:9) diluted with n-octane [TCI (Shanghai) Development Co., Ltd.] was prepared (PDMS: n-octane 3:7). Then 1 µL of the mixture was drawn into the pipette and 0.2 µL was squeezed out to form a bead. AFE was scraped with liquid beads at a constant speed several times and then placed in an 80 °C oven for 15 min to cure the insulation layer.

In Vivo Tests: The animal experimental procedures were consistent with previous reports and were repeated here for completeness.[18] All the animal experimental procedures were approved by the Ethics Committee of Fudan University (certificate number: SYXK-Hu-2020-0032) and the International Ethical Guidelines and the National Institutes of Health Guide concerning the Care and Use of Laboratory Animals were strictly followed. Electrodes were tested in male mice (ICR, 6 weeks old, Shanghai SLAC Laboratory Animal Co., Ltd., certificate number: SYXK-Hu-2022-0012) housed at ordinary animal room (12 h light/dark cycle, 22 °C, food and water ad libitum). No animals were excluded from the analysis.

Surgeries were performed on deeply anesthetized mice (2% isoflurane mixed in air) positioned in a stereotactic frame (RWD). Cefuroxime sodium (2 mg kg^{-1}) was administered subcutaneously over the shoulders to reduce the inflammatory response, followed by the subcutaneous administration of 0.5% lidocaine directly under the scalp incision site. Then the scalp was removed by scissors. An electric drill was used to remove the skull of implantation sites. One flat head screw was screwed to another side as ground and reference. All surgical instruments were sterilized.

For chronic experiments, after the electrodes were implanted as described above, bare brain tissue was covered with a layer of agar gel (1 wt.%), then with a layer of paraffin, and finally fixed electrodes to the skull with a dental resin adhesive (Super Bond C&B, SUN MEDICAL).

For immunofluorescence staining, the mice were euthanized and the brain was carefully removed. Brain tissue was fixed in paraformaldehyde solution for at least 24 h. Then put it into the dehydration kit and performed gradient dehydration with ethanol, alcohol-benzene, xylene, and paraffin in sequence. The dehydrated brain tissue was embedded in paraffin. After the paraffin solidified, the paraffin was smoothed and sliced with a microtome to a thickness of 3 µm. The slices were spread out in water and sliced. Finally, they were placed in an oven and baked at 60 °C for 2 h. Neurons were labeled with hexribonucleotide-binding protein-3 (NeuN, 1:500, GB13138-1, Servicebio); nuclei were labeled with 4′,6-diamidino-2-phenylindole (DAPI, G1012, Servicebio); astrocytes were labeled with glial fibrillary acidic protein (GFAP, 1:500, GB11096, Servicebio); microglias were labeled with ionized calcium-binding adapter molecule 1 (Iba1, 1:500, GB13105-1, Servicebio).

Electrophysiology was performed by using Cereplex Direct (Blackrock Microsystems) and data analysis was performed with the software Spike 2 (CED).

 © 2024 Wiley-VCH GmbH

16136829, 2024, 46, Downloaded from https://onlinelibrary.wiley.com/doi/10.1002/smll.202405000 by Fudan University, Wiley Online Library on [06/12/2024]. See the Terms and Conditions (https://onlinelibrary.wiley.com/terms-and-conditions) on Wiley Online Library for rules of use; OA articles are governed by the applicable Creative Commons License

Supporting Information

Supporting Information is available from the Wiley Online Library or from the author.

Acknowledgements

C.T. and K.Z. contributed equally to this work. This work was supported by NSFC (52122310, 22075050, T2321003, 22335003), MOST (2022YFA1203001, 2022YFA1203002), and CPSF (2023M740652).

Conflict of Interest

The authors declare no conflict of interest.

Data Availability Statement

The data that support the findings of this study are available in the supplementary material of this article.

Keywords

all-metal flexible fibers, continuous fabrication, fiber electronics, silver nanowires

Received: June 18, 2024
Published online: August 17, 2024

[1] a) W. Zeng, L. Shu, Q. Li, S. Chen, F. Wang, X. M. Tao, *Adv. Mater.* **2014**, *26*, 5310; b) K. Zeng, X. Shi, C. Tang, T. Liu, H. Peng, *Nat. Rev. Mater.* **2023**, *8*, 552; c) X. Xu, S. Xie, Y. Zhang, H. Peng, *Angew. Chem., Int. Ed.* **2019**, *58*, 13643.

[2] A. Fakharuddin, H. Li, F. Di Giacomo, T. Zhang, N. Gasparini, A. Y. Elezzabi, A. Mohanty, A. Ramadoss, J. Ling, A. Soultati, M. Tountas, L. Schmidt-Mende, P. Argitis, R. Jose, M. K. Nazeeruddin, A. R. B. Mohd Yusoff, M. Vasilopoulou, *Adv. Energy Mater.* **2021**, *11*, 2101443.

[3] Z. Liu, D. Qi, G. Hu, H. Wang, Y. Jiang, G. Chen, Y. Luo, X. J. Loh, B. Liedberg, X. Chen, *Adv. Mater.* **2017**, *30*, 1704229.

[4] D. Li, Z. Zhu, Z. Zhao, Y. Ji, X. Fu, Z. Liu, W. Yang, Y. Wang, *Commun. Mater.* **2023**, *4*, 28.

[5] R. Ma, B. Kang, S. Cho, M. Choi, S. Baik, *ACS Nano* **2015**, *9*, 10876.

[6] X. Yang, T. Zhou, T. J. Zwang, G. Hong, Y. Zhao, R. D. Viveros, T. M. Fu, T. Gao, C. M. Lieber, *Nat. Mater.* **2019**, *18*, 510.

[7] P. Zoio, A. Oliva, *Pharmaceutics* **2022**, *14*, 682.

[8] H. Wang, H. Tang, J. Liang, Y. Chen, *Adv. Funct. Mater.* **2018**, *28*, 1804479.

[9] M. Layani, M. Grouchko, S. Shemesh, S. Magdassi, *J. Mater. Chem.* **2012**, *22*, 14349.

[10] J. Lee, I. Lee, T. S. Kim, J. Y. Lee, *Small* **2013**, *9*, 2887.

[11] a) M. Rothe, Y. Zhao, G. Kewes, Z. Kochovski, W. Sigle, P. A. van Aken, C. Koch, M. Ballauff, Y. Lu, O. Benson, *Sci. Rep.* **2019**, *9*, 3859; b) E. C. Garnett, W. Cai, J. J. Cha, F. Mahmood, S. T. Connor, M. Greyson Christoforo, Y. Cui, M. D. McGehee, M. L. Brongersma, *Nat. Mater.* **2012**, *11*, 241; c) J. Liu, Y. Ge, D. Zhang, M. Han, M. Li, M. Zhang, X. Duan, Z. Yang, J. Hu, *ACS Appl. Nano Mater.* **2021**, *4*, 1664.

[12] a) Z. Xu, C. Gao, *Nat. Commun.* **2011**, *2*, 571; b) H. P. Cong, X. C. Ren, P. Wang, S. H. Yu, *Sci. Rep.* **2012**, *2*, 613; c) X. Zhang, Q. Li, Y. Tu, Y. Li, J. Y. Coulter, L. Zheng, Y. Zhao, Q. Jia, D. E. Peterson, Y. Zhu, *Small* **2007**, *3*, 244; d) S. Zhang, K. K. K. Koziol, I. A. Kinloch, A. H. Windle, *Small* **2008**, *4*, 1217; e) J. Zhang, S. Seyedin, S. Qin, Z. Wang, S. Moradi, F. Yang, P. A. Lynch, W. Yang, J. Liu, X. Wang, J. M. Razal, *Small* **2019**, *15*, 1804732; f) Q. Yang, Z. Xu, B. Fang, T. Huang, S. Cai, H. Chen, Y. Liu, K. Gopalsamy, W. Gao, C. Gao, *J. Mater. Chem. A.* **2017**, *5*, 22113; g) Z. Xu, Y. Liu, X. Zhao, L. Peng, H. Sun, Y. Xu, X. Ren, C. Jin, P. Xu, M. Wang, C. Gao, *Adv. Mater.* **2016**, *28*, 6449; h) G. Xin, W. Zhu, Y. Deng, J. Cheng, L. T. Zhang, A. J. Chung, S. De, J. Lian, *Nat. Nanotechnol.* **2019**, *14*, 168; i) G. Xin, T. Yao, H. Sun, S. M. Scott, D. Shao, G. Wang, J. Lian, *Science* **2015**, *349*, 1083; j) C. Xiang, C. C. Young, X. Wang, Z. Yan, C. C. Hwang, G. Cerioti, J. Lin, J. Kono, M. Pasquali, J. M. Tour, *Adv. Mater.* **2013**, *25*, 4592; k) Z. Wang, S. Qin, S. Seyedin, J. Zhang, J. Wang, A. Levitt, N. Li, C. Haines, R. Ovalle-Robles, W. Lei, Y. Gogotsi, R. H. Baughman, J. M. Razal, *Small* **2018**, *14*, 1802225; l) B. Vigolo, A. Pénicaud, C. Coulon, C. Sauder, R. Pailler, C. Journet, P. Bernier, P. Poulin, *Science* **2000**, *290*, 1331; m) J. Steinmetz, M. Glerup, M. Paillet, P. Bernier, M. Holzinger, *Carbon* **2005**, *43*, 2397; n) S. Seyedin, E. R. S. Yanza, J. M. Razal, *J. Mater. Chem. A* **2017**, *5*, 24076; o) L. M. Ericson, H. Fan, H. Peng, V. A. Davis, W. Zhou, J. Sulpizio, Y. Wang, R. Booker, J. Vavro, C. Guthy, A. N. G. Parra-Vasquez, M. J. Kim, S. Ramesh, R. K. Saini, C. Kittrell, G. Lavin, H. Schmidt, W. W. Adams, W. E. Billups, M. Pasquali, W. F. Hwang, R. H. Hauge, J. E. Fischer, R. E. Smalley, *Science* **2004**, *305*, 1447; p) W. Eom, H. Shin, R. B. Ambade, S. H. Lee, K. H. Lee, D. J. Kang, T. H. Han, *Nat. Commun.* **2020**, *11*, 2825; q) V. A. Davis, A. N. G. Parra-Vasquez, M. J. Green, P. K. Rai, N. Behabtu, V. Prieto, R. D. Booker, J. Schmidt, E. Kesselman, W. Zhou, H. Fan, W. W. Adams, R. H. Hauge, J. E. Fischer, Y. Cohen, Y. Talmon, R. E. Smalley, M. Pasquali, *Nat. Nanotechnol.* **2009**, *4*, 830.

[13] C. Boehler, S. Carli, L. Fadiga, T. Stieglitz, M. Asplund, *Nat. Protoc.* **2020**, *15*, 3557.

[14] Y. Liu, J. Liu, S. Chen, T. Lei, Y. Kim, S. Niu, H. Wang, X. Wang, A. M. Foudeh, J. B. H. Tok, Z. Bao, *Nat. Biomed. Eng.* **2019**, *3*, 58.

[15] S. Choi, S. I. Han, D. Jung, H. J. Hwang, C. Lim, S. Bae, O. K. Park, C. M. Tschabrunn, M. Lee, S. Y. Bae, J. W. Yu, J. H. Ryu, S. W. Lee, K. Park, P. M. Kang, W. B. Lee, R. Nezafat, T. Hyeon, D. H. Kim, *Nat. Nanotechnol.* **2018**, *13*, 1048.

[16] C. Zhao, P. Zhang, J. Zhou, S. Qi, Y. Yamauchi, R. Shi, R. Fang, Y. Ishida, S. Wang, A. P. Tomsia, M. Liu, L. Jiang, *Nature* **2020**, *580*, 210.

[17] C. Luan, Y. Shao, Q. Lu, S. Gao, K. Huang, H. Wu, K. Yao, *ACS Appl. Mater. Interfaces* **2018**, *10*, 17950.

[18] a) C. Tang, S. Xie, M. Wang, J. Feng, Z. Han, X. Wu, L. Wang, C. Chen, J. Wang, L. Jiang, P. Chen, X. Sun, H. Peng, *J. Mater. Chem. B.* **2020**, *8*, 4387; b) J. Feng, Y. Fang, C. Wang, C. Chen, C. Tang, Y. Guo, L. Wang, Y. Yang, K. Zhang, J. Wang, J. Chen, X. Sun, H. Peng, *Adv. Funct. Mater.* **2023**, *33*, 2214945.

 © 2024 Wiley-VCH GmbH

16136829, 2024, 46, Downloaded from https://onlinelibrary.wiley.com/doi/10.1002/smll.202405000 by Fudan University, Wiley Online Library on [06/12/2024]. See the Terms and Conditions (https://onlinelibrary.wiley.com/terms-and-conditions) on Wiley Online Library for rules of use; OA articles are governed by the applicable Creative Commons License